

Engineering the Structural and Electronic Phases of MoTe_2 through W Substitution

D. Rhodes,^{†,‡} D. A. Chenet,[§] B. E. Janicek,^{||} C. Nyby,[⊥] Y. Lin,[#] W. Jin,[#] D. Edelberg,[▽] E. Mannebach,[○] N. Finney,[§] A. Antony,[§] T. Schiros,^{◆,¶} T. Klarr,[◆] A. Mazzoni,[◆] M. Chin,[◆] Y.-c. Chiu,^{†,‡} W. Zheng,^{†,‡} Q. R. Zhang,^{†,‡} F. Ernst,^{●,■} J. I. Dadap,[■] X. Tong,[★] J. Ma,[▲] R. Lou,[◇] S. Wang,[◇] T. Qian,[▲] H. Ding,[▲] R. M. Osgood, Jr.,^{■,■} D. W. Paley,^{○,□} A. M. Lindenberg,^{○,●,□} P. Y. Huang,[★] A. N. Pasupathy,[▽] M. Dubey,[◆] J. Hone,[§] and L. Balicas^{*,†,Ⓢ}

[†]National High Magnetic Field Laboratory, Florida State University, Tallahassee, Florida 32310, United States

[‡]Department of Physics, Florida State University, Tallahassee, Florida 32306, United States

[§]Department of Mechanical Engineering, Columbia University, New York, New York 10027, United States

^{||}Department of Materials Science and Engineering, University of Illinois Urbana–Champaign, Urbana, Illinois 61801, United States

[⊥]Department of Chemistry, Stanford University, Stanford, California 94305-4401, United States

[#]Department of Applied Physics and Applied Mathematics and [▽]Department of Physics, Columbia University, New York, New York 10027, United States

[○]Department of Materials Science and Engineering, Stanford University, Stanford, California 94305, United States

[◆]Materials Research Science and Engineering Center, Columbia University, New York, New York 10027 United States

[¶]Department of Science and Mathematics, SUNY Fashion Institute of Technology, New York, New York 10001 United States

[◆]Sensors and Electronic Devices Directorate, United States Army Research Laboratory, Adelphi, Maryland 20723, United States

[●]Department of Applied Physics, Stanford University, Stanford, California 94305-4090, United States

[■]Stanford PULSE Institute, SLAC National Accelerator Laboratory, Menlo Park, California 94025, United States

[■]Department of Electrical Engineering, Columbia University, New York, New York 10027, United States

[★]Center for Functional Nanomaterials, Brookhaven National Laboratory, Upton, New York 11973-5000, United States

[▲]Beijing National Laboratory for Condensed Matter Physics, and Institute of Physics, Chinese Academy of Sciences, Beijing 100190, China

[◇]Department of Physics, Renmin University of China, Beijing 100872, China

[○]Department of Chemistry and [□]Columbia Nano Initiative, Columbia University, New York, New York 10027, United States

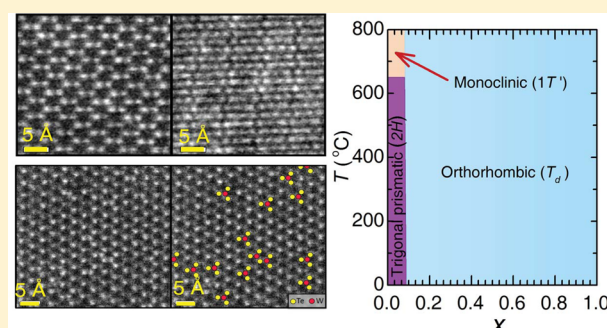
[□]Stanford Institute for Materials and Energy Sciences, SLAC National Accelerator Laboratory, Menlo Park, California 94025, United States

[★]Department of Mechanical Science and Engineering, University of Illinois Urbana–Champaign, Urbana, Illinois 61801, United States

Supporting Information

ABSTRACT: MoTe_2 is an exfoliable transition metal dichalcogenide (TMD) that crystallizes in three symmetries: the semiconducting trigonal-prismatic 2H- or α -phase, the semimetallic and monoclinic 1T'- or β -phase, and the semimetallic orthorhombic γ -structure. The 2H-phase displays a band gap of ~ 1 eV making it appealing for flexible and transparent optoelectronics. The γ -phase is predicted to possess unique topological properties that might lead to topologically protected nondissipative transport channels. Recently, it was argued that it is possible to locally induce phase-transformations in TMDs, through chemical doping, local heating, or electric-field to achieve ohmic contacts or to induce

continued...



Received: November 17, 2016

Revised: January 30, 2017

Published: February 1, 2017

useful functionalities such as electronic phase-change memory elements. The combination of semiconducting and topological elements based upon the same compound might produce a new generation of high performance, low dissipation optoelectronic elements. Here, we show that it is possible to engineer the phases of MoTe_2 through W substitution by unveiling the phase-diagram of the $\text{Mo}_{1-x}\text{W}_x\text{Te}_2$ solid solution, which displays a semiconducting to semimetallic transition as a function of x . We find that a small critical W concentration $x_c \sim 8\%$ stabilizes the γ -phase at room temperature. This suggests that crystals with x close to x_c might be particularly susceptible to phase transformations induced by an external perturbation, for example, an electric field. Photoemission spectroscopy, indicates that the γ -phase possesses a Fermi surface akin to that of WTe_2 .

KEYWORDS: Transition-metal-dichalcogenides, phase-transformations, Weyl semimetals, electron microscopy, Raman spectroscopy, photoemission spectroscopy

The properties of semiconducting and of semimetallic MoTe_2 are of fundamental interest in their own right^{1–4} but also for their potential technological relevance. In the mono- or few-layer limit, it is a direct-gap semiconductor, while the bulk has an indirect bandgap^{5–7} of ~ 1 eV. The size of the gap is similar to that of Si, making 2H- MoTe_2 particularly appealing for both purely electronic devices^{8,9} and optoelectronic applications.¹⁰ Moreover, the existence of different phases opens up the possibility for many novel devices and architectures. For example, controlled conversion of the $1\text{T}'$ - MoTe_2 phase to the 2H-phase, as recently reported,¹¹ could enable circuits composed of a single material functioning as both semiconducting channels and metallic interconnects. More precise control of the phase change might also be used to minimize the metal–semiconductor Schottky barrier by continuous evolution of the electronic band structure in order to overcome current limits on optoelectronic performance.¹² In fact, recent work has reported contact phase engineering by laser processing¹³ and chemical modification.¹⁴

The ability to phase-engineer MoTe_2 has many broader applications and potentially deeper implications. For instance, doping, temperature, strain, and electric fields can be used to drive metal-to-insulator transitions^{15–19} for sensors and non-volatile information storage. More fundamentally, the electronic structure of monolayers of semimetallic MoTe_2 (and of WTe_2) has been proposed to possess a Z_2 topological invariant characteristic of a quantum spin Hall-effect ground-state which has a gap in the bulk and nondissipative edge states.²⁰ If confirmed,⁴ these edge states could be used for dissipation-free nanointerconnects between logical elements based on semiconducting 2H- MoTe_2 for low-power electronics. More recent theoretical developments also claim that both orthorhombic MoTe_2 and WTe_2 would be candidates for a new type of Weyl semimetallic state characterized by linear touching points between hole- and electron-Fermi surfaces, where the Berry-phase would present topological singularities.^{21–26} These singularities, which were recently claimed to have been observed in the orthorhombic phase of MoTe_2 ,²⁷ could lead to unconventional transport properties.

To fully control and utilize phase transitions in the two-dimensional (2D) tellurides, it is crucial to understand the phase diagram in detail. In particular, doping of the lattice can be used to precisely tune the semiconducting-metallic phase transition, and in fact W doping is known to induce a phase transition¹⁸ from the 2H- to an orthorhombic structure, originally identified as the $1\text{T}'$ -phase, in $\text{Mo}_{1-x}\text{W}_x\text{Te}_2$. Early studies identified a structural phase-transition from 2H to orthorhombic for $x > 0.15$ and with a zone of phase coexistence for $0.15 < x < 0.34$.²⁸ However, given the renewed interest in this material, there is strong motivation to revisit the question of the precise evolution of the phases in the 2D tellurides with doping.

Here, we synthesize bulk crystals of $\text{Mo}_{1-x}\text{W}_x\text{Te}_2$ alloys and characterize their composition and structure through a combination of techniques including electron microscopy, X-ray diffraction, scanning tunneling microscopy, and Raman spectroscopy. We find that W doping produces homogeneous alloys with no phase coexistence as previously observed.²⁸ The structural phase transition from the semiconducting 2H-phase toward the orthorhombic and semimetallic γ -phase is sharp and occurs at a modest critical molar fraction $x_c \sim 0.08$. Because crystals with $x \lesssim x_c$ are likely to be susceptible to small perturbations such as strain or electric field, this opens the possibility of reversibly controlling the structural, and therefore electronic properties, of the $\text{Mo}_{1-x}\text{W}_x\text{Te}_2$ series. Additionally, we show through angle-resolved photoemission spectroscopy that the geometry of the Fermi surface of γ - $\text{Mo}_{1-x}\text{W}_x\text{Te}_2$ is remarkably similar to that of WTe_2 , thus confirming its semimetallic character.

Single crystals of the $\text{Mo}_{1-x}\text{W}_x\text{Te}_2$ series were grown through a chemical vapor transport technique as described in the [Supporting Information](#). Unless otherwise noted, samples were cooled slowly in order to obtain the equilibrium phase at room temperature. Their precise stoichiometry was determined through energy dispersive X-ray spectroscopy (EDS) and photoelectron spectroscopy (XPS), see [SI](#) as well as Figure S1 for photoelectron core level spectrum of a $\text{Mo}_{1-x}\text{W}_x\text{Te}_2$ crystal and Figure S2 for details concerning the determination of the W content ($x \pm 0.01$). Stoichiometric MoTe_2 ($x = 0$) and WTe_2 ($x = 1$) were synthesized through a Te flux method. For MoTe_2 , samples were slowly cooled to yield the 2H-phase or quenched to room temperature to yield the metastable $1\text{T}'$ -phase.

Figure 1 shows structural analysis via single crystal X-ray diffraction (XRD), scanning transmission electron microscopy (STEM), and scanning tunneling microscopy (STM). For STEM, the crystals were exfoliated following a standard procedure and transferred onto a TEM grid, see [SI](#). Figure 1a,b displays atomic resolution STEM images collected from two distinct multilayered crystals with compositions of $\text{Mo}_{0.93}\text{W}_{0.07}\text{Te}_2$ and $\text{Mo}_{0.87}\text{W}_{0.13}\text{Te}_2$, respectively. These crystals display distinct crystallographic structures: $x \simeq 0.07$ shows the hexagonal pattern characteristic of the trigonal prismatic or the 2H- phase, while $x \simeq 0.13$ shows a striped pattern consistent with either the $1\text{T}'$ - or the γ -phase. In Figure S3, we have included STEM and electron diffraction images for $x \simeq 0.13$ from whose analysis we conclude that it crystallizes in the orthorhombic γ -phase. Nevertheless, in Figure 1c,d we also show single-crystal XRD patterns for $x = 0.0$ and $x = 0.27$, respectively. Analysis of these patterns confirms that crystals with $x \lesssim 0.07$ crystallize in the 2H-phase, whereas crystals with $x > 0.07$, in this case $x = 0.27$, display the orthorhombic γ -phase instead of the monoclinic $1\text{T}'$ -one. Figure S4 shows X-ray diffraction patterns for $\text{Mo}_{0.91}\text{W}_{0.09}\text{Te}_2$ and $\text{Mo}_{0.82}\text{W}_{0.18}\text{Te}_2$, also indicating the γ -phase for these concentrations.

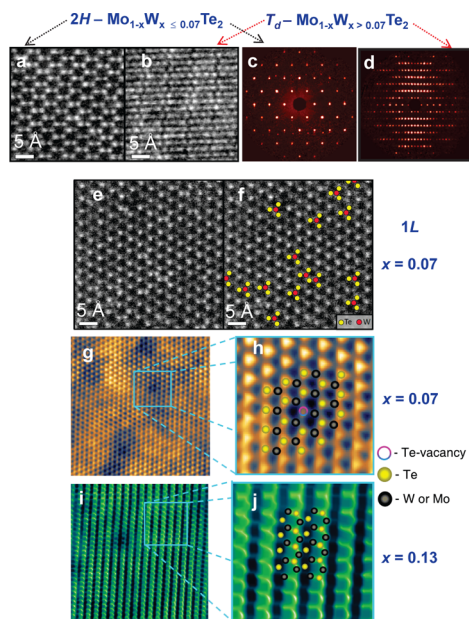


Figure 1. (a) Scanning transmission electron microscopy image of a few-layered crystal of $\text{Mo}_{1-x}\text{W}_x\text{Te}_2$ with $x \approx 0.07\%$ displaying the hexagonal pattern typical of the 2H- or trigonal prismatic phase. (b) STEM image of a few-layered crystal of $\text{Mo}_{1-x}\text{W}_x\text{Te}_2$ with $x \approx 0.13$. Notice that its atomic arrangement is no longer consistent with the 2H-phase. All STEM images are lightly smoothed. (c) Single-crystal X-ray diffraction pattern for $x = 0.0$ ($hk0$) indicating that it crystallizes in the 2H-phase. (d) Single-crystal X-ray diffraction pattern for $x = 0.27$ ($0kl$) indicating that it crystallizes in the γ -phase (orthorhombic $Pmn2_1$). Powder X-ray diffraction indicates that for $x > 0.08$ the $\text{Mo}_{1-x}\text{W}_x\text{Te}_2$ series crystallizes in the γ -phase. (e) $(8.25 \text{ nm})^2$ area STEM image of monolayer $2\text{H-Mo}_{1-x}\text{W}_x\text{Te}_2$. (f) Brighter W atoms (indicated by red dots) are identifiable through their contrast with respect to the darker Mo atoms. Therefore, STEM indicates that these crystals are homogeneous solid-solutions containing Mo and W atoms. (g) Scanning tunneling microscopy image of a $\text{Mo}_{1-x}\text{W}_x\text{Te}_2$ single crystal with $x = 0.07$, corresponding to an area of $(15 \text{ nm})^2$ and showing a clear hexagonal pattern as expected for the 2H-phase. The spatial modulation in intensity reflects modulations in the local density of states which depend on the local coupling between the top and the adjacent layers and implies that the interplanar coupling is nonuniform. (h) Magnification of a local area of $(2.5 \text{ nm})^2$ where one can detect a Te vacancy. (i) STM image of an $x = 0.13$ single-crystal, also corresponding to an area of $(15 \text{ nm})^2$, showing a pattern of parallel chains as expected for the orthorhombic γ -phase. (j) Magnification of a local region of $(2.5 \text{ nm})^2$ revealing the intrachain structure and illustrating the crystallographic positions of transition metal (black dots) and Te (yellow dots) atoms, respectively.

Our complete set of structural studies indicate that for all concentrations $x > x_c = 0.08$, W doping stabilizes the semimetallic γ -phase, confirming that the structural transition is sharp and occurs at a W doping level significantly lower than previously reported.²⁸ Figure 1e shows a larger-scale STEM image of $\text{Mo}_{0.93}\text{W}_{0.07}\text{Te}_2$. In this image, bright dots surrounded by three additional dots (Te atoms) correspond to randomly distributed W atoms, as highlighted in Figure 1f. Therefore, the STEM images clearly indicate that the $\text{Mo}_{1-x}\text{W}_x\text{Te}_2$ series results from a homogeneous dilution of W atoms into a MoTe_2 matrix and not from the coexistence of 2H-MoTe_2 and WTe_2 domains. This lack of phase coexistence is further confirmed by room-temperature STM imaging of vacuum-cleaved crystals, as shown in Figure 1g,h. For $x = 0.07$, see Figure 1g, the equidistant distribution of Te atoms around the transition metal(s) forming an angle of $\theta = 120^\circ$

among them, indicates unambiguously the trigonal prismatic coordination of the 2H-phase. In contrast, for $x = 0.13$, see Figure 1i,j, rows of atoms indicate a change in symmetry from triangular to (nearly) rectangular at the surface. In amplified images, for example, Figure 1h, one can clearly discern Te vacancies (indicated by a multicolored dot). Therefore, we have enough resolution to observe vacancies but we do not observe the coexistence of distinct crystallographic phases.

Thus, TEM, STM, and XRD analyses yield consistent results, namely a transition from the 2H-phase to the orthorhombic phase at $x_c \sim 0.08$ with no phase coexistence even near the phase boundary. These observations stand in contrast to the early work in ref 28, which reported a higher critical W concentration and a region of phase coexistence near the boundary. This discrepancy is likely attributable to the difference between the methods of synthesis used for each study; in our case the use of higher temperatures, a transport agent and a longer synthesis time should lead to a more homogeneous material. Having established the room-temperature phase boundary between the 2H and the orthorhombic transition, we now turn to the temperature axis of the phase-diagram.

The structural phase transition as a function of doping is accompanied by changes in vibrational modes, as probed by Raman spectroscopy (see Figure 2). Figure 2a shows

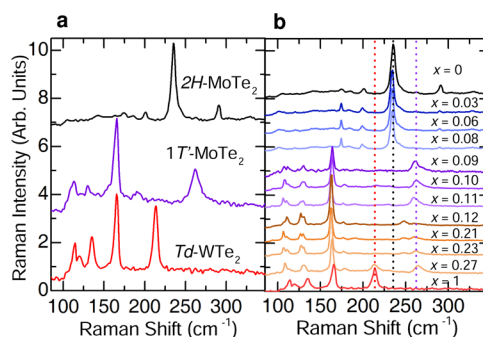


Figure 2. (a) Raman spectra for bulk 2H-MoTe_2 (black trace), bulk $1\text{T}'\text{-MoTe}_2$ (blue), and bulk $\gamma\text{-WTe}_2$ (red) at room temperature using an excitation wavelength of 532 nm. (b) Raman spectra of $\text{Mo}_{1-x}\text{W}_x\text{Te}_2$ for several values of x (fraction of W). Notice the change in the spectrum observed for $x \geq 0.09$, indicating a structural phase-transition as a function of doping.

room-temperature Raman spectra obtained from the 2H- and $1\text{T}'\text{-MoTe}_2$ phases and from WTe_2 . The 2H-structure displays two main Raman peaks at 174 and 235 cm^{-1} corresponding to the A_{1g} and E_g^1 modes, respectively.^{8,29} Reflecting its reduced symmetry, the $1\text{T}'$ phase displays several peaks at lower wavenumbers. For this structure the main peaks occur at 163 and 260 cm^{-1} and have been indexed as the B_g and A_g modes,⁴ respectively. WTe_2 presents a spectrum having peaks occurring at 136 and 165 cm^{-1} respectively, both of A_g character³⁰ in addition to a peak at $\sim 210 \text{ cm}^{-1}$ previously indexed as the A_g^2 mode. In Figure S6, we show Raman spectra for $\gamma\text{-Mo}_{0.88}\text{W}_{0.12}\text{Te}_2$ as the number of layers decrease, indicating that the γ -phase is stable down to the single-layer limit despite its high Mo content. Figure 2b shows Raman spectra for several stoichiometries of the $\text{Mo}_{1-x}\text{W}_x\text{Te}_2$ series. $\text{Mo}_{1-x}\text{W}_x\text{Te}_2$ crystallizes in the 2H-phase for concentrations up to $x \sim 0.08$. For concentrations beyond this value, the spectra abruptly change, as indicated by the disappearance of the A_{1g} and of the E_{2g}^1 peaks at 174 and 235 cm^{-1} , respectively, which are observed when $x \leq 0.08$. These data support the conclusions reached by the structural probes

above, namely a phase transition around $x_c \sim 0.08$ with no evidence for phase coexistence. Interestingly, as the W concentration increases beyond $x = 0.08$, we see the emergence of peaks that at the first glance would seem to be related to the B_g and the A_g modes of the $1T'$ -phase.⁴ However, single-crystal X-ray diffraction shown in Figure 1d and in Figure S3 clearly indicates that the Raman spectra in Figure 2b must be associated with the orthorhombic γ -phase with certain peaks shifted with respect to those of WTe_2 due to the high Mo content. An important observation is that Raman scattering yields nearly identical spectra for $1T'$ - $MoTe_2$ and for γ - $Mo_{1-x}W_xTe_2$ for reasons that will have to be clarified through theoretical calculations. We note that this similarity might lead to misidentification of the $1T'$ -phase if Raman spectroscopy is the only method used to probe the crystal structure. In Figure S7, we have included transport data, like the room-temperature conductivity as a function of doping, which changes by orders of magnitude as one crosses the phase-boundary.

Next, we investigated the electronic phase-transition accompanying the structural phase transition. In particular, while the nature of the semiconducting 2H-phase is well understood, it is not known whether the orthorhombic phase in the W-doped material is a conventional or a Weyl semimetallic system. Therefore, we investigated the electronic structure of heavily doped $Mo_{1-x}W_xTe_2$ single crystals through angle-resolved photoemission spectroscopy (ARPES), as shown in Figure 3. The core level spectrum, shown in the Figure S1, displays the characteristic peaks of W and Te elements, confirming that W is alloyed into the $1T'$ - $MoTe_2$ crystal. As seen in Figure S1, the W 4f core levels have one set of doublets at 31.4 and 33.6 eV (right

inset in Figure S1) respectively, in perfect agreement with the values found in the literature.³¹ Meanwhile the Te $4d_{5/2}$ and $4d_{3/2}$ doublets split into four peaks (left inset in Figure S1). This suggests that the Mo/W layer is sandwiched by the Te layers, making the Te layer the exposed surface. To investigate the electronic structure along the k_z -direction of the three-dimensional Brillouin zone (BZ), which is depicted in Figure 3a, we performed photon-energy-dependent ARPES measurements with energies ranging from 40 to 90 eV. Figure 3b shows the ARPES spectra at the Fermi level E_F as a function of the momentum and photon energy from 55 to 75 eV. We extracted the positions of the Γ ($k_z = 0$) and Z ($k_z = \pi$) points from the dispersion as a function of k_z , as shown. Figure 3c shows the Fermi surface of $Mo_{0.73}W_{0.27}Te_2$ acquired at $h\nu = 70$ eV. The Fermi surface along the $Y-\Gamma-Y$ direction shows two hole-pockets and two-electron pockets at either side of Γ which would seem to touch. This geometry for the Fermi surface of $Mo_{0.73}W_{0.27}Te_2$ (as well as its overall electronic band-structure) is remarkably similar to the one reported in ref 32 for WTe_2 and therefore remarkably different from the one already reported²⁷ for orthorhombic $MoTe_2$. This difference is particularly striking given its considerably larger content of Mo relative to W. Notice that such a simple Fermi surface would be in broad agreement with our recent study³³ on the quantum oscillatory phenomena observed in γ - $MoTe_2$.

ARPES band-maps along the high symmetry directions of a $Mo_{0.73}W_{0.27}Te_2$ single crystal, as well as the corresponding plots of their second derivatives, are shown in Figure 3d–h. Figure 3d,f shows band-maps and corresponding second derivative, acquired with a photon energy of 70 eV ($k_z = 0$) along the $Y-\Gamma-Y$

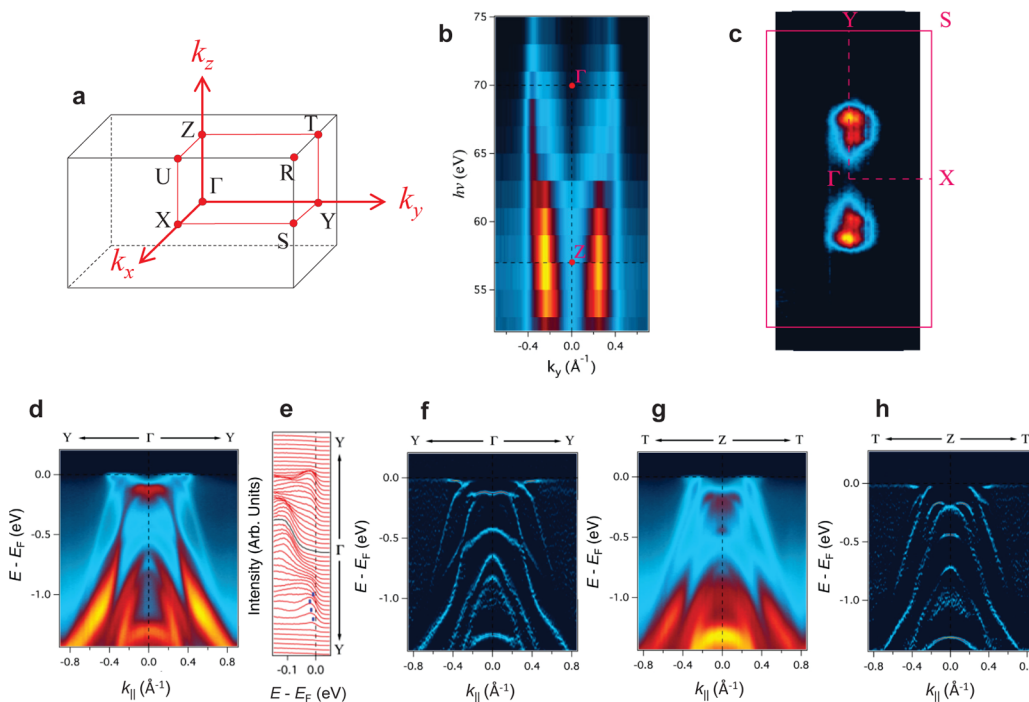


Figure 3. (a) Bulk Brillouin zone of $Mo_{0.73}W_{0.27}Te_{1.99}$ indicating its high symmetry points. (b) ARPES intensity plot at the Fermi level as a function of both the momentum and the photon energy. (c) Topography of the Fermi surface at $k_z = 0$. One electron- and one hole-like pocket is observed at either side of the Γ -point. The resolution of our ARPES measurements limits our ability to identify possible points of contact between the electron and the hole pockets. (d) ARPES band structure along $Y-\Gamma-Y$ direction acquired with a photon energy of 70 eV, that is, corresponding to ($k_z = 0$). (e) Plot of the energy distribution curve of the low energy bands. Blue dotted line serves as a guide to the eye, indicating the positions of peaks for the electron-like band. (f) Second derivative of the band structure collected along the $Y-\Gamma-Y$ direction. (g) ARPES band structure along $T-Z-T$ direction acquired with a photon energy of 57 eV, that is, corresponding to ($k_z = \pi$). (h) Second derivative of the band structure collected along the $T-Z-T$ direction.

direction. Figures 3g,h correspond, respectively, to band maps and second derivatives collected along the T–Z–T direction with a photon energy of 57 eV corresponding to ($k_z = \pi$). The remarkable features near E_F are the flat hole-like band crossing E_F around $k_{||} \sim 0.2 \text{ \AA}^{-1}$, and an electron-like pocket in the vicinity of $k_{||} \sim 0.4 \text{ \AA}^{-1}$. The band connecting the hole- and the electron-like pockets is assigned to a surface state, which has already been claimed to be topologically nontrivial.^{26,34} When compared to the calculations in ref 26, the conduction band minimum is observed to be very close to the Fermi level, which makes this surface state not as easily detectable as one would expect from the calculations. The surface state is more clearly exposed in Figure S8. Notice that the bands near E_F at $k_z = 0$ have higher binding energies than those at $k_z = \pi$. As a result, the electron pocket and the surface state become more apparent in Figures 3d,f.

Having established the room-temperature boundary between the 2H- and γ -phases and explored the electronic structure of the latter phase, we now turn to the temperature axis of the phase-diagram. Figure 4 shows powder XRD patterns for a sample with

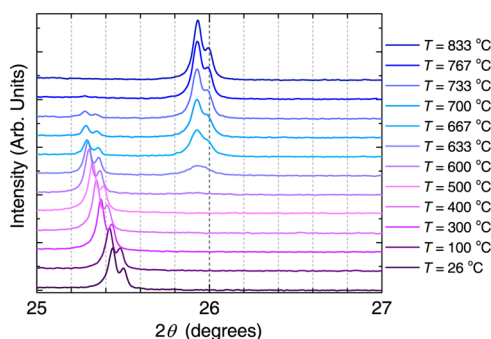


Figure 4. Powder X-ray diffraction as a function of angle for 2H-Mo_{0.95}W_{0.05}Te₂. Notice the disappearance of the peaks associated with the 2H-phase and the emergence of new peaks, above $T = 600^\circ\text{C}$ which can be ascribed to the 1T'-phase. In a certain range of temperatures, the coexistence of Bragg reflections associated with both phases results from the coexistence of domains and indicates a first-order phase-transition.

$x \approx 0.05$, at different temperatures upon heating from room temperature. Above $T = 600^\circ\text{C}$, the peaks associated with the 2H-phase disappear and new peaks that can be ascribed to the 1T'-phase appear. Similar studies for different compositions are shown in Figure S5. We find that the boundary is situated at $T_{2\text{H}-1\text{T}'} \sim 650^\circ\text{C}$ with a large, sample dependent uncertainty of the order of $\sim 50^\circ\text{C}$ previously attributed to variations in the Te stoichiometry.⁴ The variation of $T_{2\text{H}-1\text{T}'}$ as a function of x remains within this uncertainty, therefore the boundary should be considered as doping independent. Domains or phase coexistence⁴ is clearly observed only for $x \leq 0.08$ and under temperatures ranging from ~ 630 to $\sim 730^\circ\text{C}$. Notice that a similar coexistence is observed also for $x = 0$, see Figure S5, indicating that it does not result from W doping. The 1T'-MoTe₂ phase continues to display a good degree of crystallinity at high temperatures indicating that the structural transition is not driven by an increase in the number of Te vacancies or material degradation. For $x > 0.08$, we could not detect additional phase transitions as a function of either x or T .

The proposed phase diagram, shown in Figure 5, depicts a sharp phase-boundary between the 2H- and the orthorhombic phases at $x_c \sim 0.08$, and the boundary between the 2H- and 1T'- phases at $\sim 650^\circ\text{C}$. In Figure S9, we compare X-ray powder diffraction data among samples crystallizing in the 2H- and in the γ -phases and the role of the temperature. The important point is

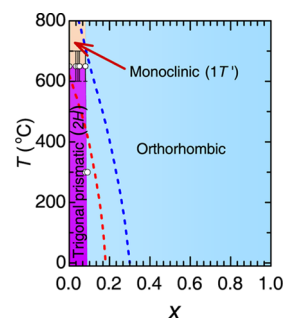


Figure 5. Bulk phase-diagram of the Mo_{1-x}W_xTe₂ series based on the array of experimental techniques used for this study. The phase-boundary between the 2H-, 1T', and the orthorhombic phases were determined through powder X-ray diffraction measurements as a function of T and x up to $x = 0.13$. Above 800°C , the samples decompose or lose their crystallinity. The error bars in x , inherent to the EDS and the XPS techniques, are in the order of 1% therefore not clearly observable in the plot. Red and blue lines depict the metastable phase-boundary predicted by ref 18 for single-layers assuming a relaxed lattice either in the presence or in the absence of spin–orbit coupling, respectively. See main text for related discussion.

that in contrast to the 2H-phase, and even for samples with a W concentration very close to the critical one, we could not detect a structural phase-transition as a function of T in samples crystallizing in the orthorhombic-phase. Given that the orthorhombic γ -phase becomes the ground state of 1T'-MoTe₂ and the larger area occupied by it in the phase diagram, one is led to conclude that it is thermodynamically more stable than the latter phase. The most remarkable feature of the phase diagram is the very small concentration in W required to stabilize the orthorhombic semimetallic γ - phase, and not the coexistence of the 2H- and the 1T'- phases as predicted by ref 18, through a sharp boundary situated at $x = 0.08 \pm 0.01$. Such a sharp boundary points to a first-order phase-transition as a function of doping with the caveat that we could not detect phase coexistence. The large error bars for the temperature defining the boundary between the 2H- and the 1T'- phases reflects the fact that the exact transition temperature is sample dependent, possibly due to fluctuations in the Te concentration⁴ or in the density of vacancies, because the phase-transition might nucleate around the defects. Here, a few words are required concerning phases in thermodynamic equilibrium versus metastable ones: upon W doping, ref 18 predicts that the thermodynamically stable phase is characterized by the coexistence of domains belonging to both the 2H- and the 1T'- phases in agreement with observations in ref 28. Reference 18 also predicts that a sharp phase boundary between both phases is only possible if they are metastable. For the sake of comparison, we have included a red and a blue line in the phase-diagram depicting the metastable phase-boundary predicted by ref 18 for a relaxed lattice in either the presence or the absence of spin–orbit coupling, respectively. However, the entire set of experimental results reported here indicate the absence of domains quite clearly which, according to ref 18, would point to metastability. Nevertheless, our samples were not only reacted at much higher temperatures but were synthesized for a considerably longer time than those in ref 28, a procedure that leads to the correct, thermodynamically stable phase of MoTe₂, that is, the 2H-phase. Some of the doped crystals analyzed by STEM were synthesized a year earlier and yet did not reveal any evidence for the emergence of domains or for evolution as a function of time. Therefore, our experimental observations suggest that either the observed phases and their concomitant

phase-boundaries are the thermodynamically stable ones or that the characteristic time scales involved in the phase separation process¹⁸ are very long. However, to settle this issue we intend to resynthesize these alloys over an extended period of time, for example, one year instead of a few weeks to cool the crystals down to room temperature in order to proceed with a detailed structural analysis.

It is quite remarkable that a semiconducting band gap as large as ~ 1 eV⁵ for 2H-MoTe₂ can be entirely suppressed by substituting just $x_c \simeq 9 \pm 1\%$ of Mo for W which stabilizes a semimetallic state, as clearly indicated by angle-resolved photoemission experiments. Here, the situation bears a certain resemblance with the transition metal oxides such as the cuprates, whose charge- or Mott-gap is estimated to be $\Delta \sim 2$ eV, but where a small concentration of dopants, in the order of 5%, is enough to stabilize a metallic state (albeit anomalous) and even superconductivity.³⁵ This clearly indicates that both the structural and the concomitant electronic phases of MoTe₂ are particularly susceptible to small perturbations. This suggests that it should be possible to reversibly induce structural-transitions through the application of strain¹⁸ or an electric field,¹⁷ particularly in 2H-Mo_{1-x}W_xTe₂ crystals with $x \lesssim x_c$. This would make the 2H-Mo_{1-x}W_xTe₂ series particularly appealing for the development of phase-change memory devices¹⁵⁻¹⁹ or for a new generation of optoelectronic devices, whose metallic interconnects could be created or “erased” at will through the application of an electrical signal, instead of a chemical treatment. Finally, the fact that the Mo_{1-x}W_xTe₂ series produce homogeneous alloys is not only a major result of this study, but opens the unique possibility of exploring the evolution of their predicted topological/electronic properties²⁶ and of perhaps detecting topological phase-transitions in the bulk as well as in the surface state through the evolution of the Fermi surface. In effect, ARPES indicates that the Fermi surfaces of γ -MoTe₂ (ref 27) and of γ -Mo_{1-x}W_xTe₂ (this work) are remarkably different, a fact that can only be reconciled with an electronic/topological phase-transition as a function of W doping. Because W doping tends to stabilize the γ -phase, it is reasonable to expect that one can stabilize it also in samples containing small amounts of W by quickly cooling these crystals to room temperature during the synthesis process. This would produce a phase-diagram not containing the region originally occupied by the 2H-phase. This set of orthorhombic samples would allow us to explore the evolution of the Fermi surface as a function of W doping to understand, for example, how the large hole-pocket seen by ARPES at the center of the Brillouin zone²⁷ in γ -MoTe₂ disappears to originate the hole-pockets seen by us at either side of zone center in γ -Mo_{1-x}W_xTe₂. Such electronic phase-transition should lead to either the suppression or the displacement of the Weyl-points already seen by ARPES, or to a concomitant topological phase-transition as a function of W doping.

■ ASSOCIATED CONTENT

● Supporting Information

The Supporting Information is available free of charge on the ACS Publications website at DOI: 10.1021/acs.nanolett.6b04814.

Methods, photoelectron core level spectrum of a Mo_{1-x}W_xTe₂ single-crystal, determination of the W content through photoelectron spectroscopy, STEM and electron diffraction images for a γ -Mo_{0.87}W_{0.13}Te₂ single-crystal, single-crystal X-ray diffraction patterns for $x = 0.09$ and

0.18, powder X-ray diffraction for single-crystals with $x \leq 0.05$ as a function of the temperature, Raman spectra for γ -Mo_{0.88}W_{0.12}Te₂ as a function of the wavenumber and of the number of layers, room temperature electrical transport properties for $x = 0.03$ and $x > 0.1$, ARPES momentum distribution curves and corresponding second derivative plots of their low energy bands for a $x = 0.3$ single-crystal, powder X-ray diffraction data for crystals with $x \simeq 0.05$ and $\simeq 0.08$ at distinct temperatures (PDF)

■ AUTHOR INFORMATION

Corresponding Author

*E-mail: balicas@magnet.fsu.edu.

ORCID

E. Mannebach: 0000-0002-1236-187X

L. Balicas: 0000-0002-5209-0293

Author Contributions

D.R. and D.A.C. contributed equally to this work.

Notes

The authors declare no competing financial interest.

■ ACKNOWLEDGMENTS

The subsequent order of authorship does not reflect the relative importance among the contributions from the different authors and groups. Their contributions to this work should be considered of equal relevance. L.B. is supported by the U.S. Army Research Office MURI Grant W911NF-11-1-0362. This work was supported in part by the Molecular and Electronic Nanostructures theme of the Beckman Institute at UIUC. Electron microscopy work was performed at the Frederick Seitz Materials Research Laboratory Central Research Facilities, University of Illinois. Single-crystal X-ray diffraction was performed in the Shared Materials Characterization Laboratory at Columbia University. A.M.L. acknowledges support by the U.S. Department of Energy, Basic Energy Sciences, Materials Sciences and Engineering Division. The work of R.M.O., J.L.D., W.J., and Y.L. was financially supported by the U.S. Department of Energy under Contract No. DE-FG 02-04-ER-46157. F.E. gratefully acknowledges Grant LPDS 2013-13 from the German National Academy of Sciences Leopoldina. This work was also supported by the DOE-BES, Materials Sciences and Engineering Division under Contract DE-AC02-76SF00515 and by the W. M. Keck Foundation and the Gordon and Betty Moore Foundation's EPIQS Initiative through Grant GBMF4545. D.C., N.F., A.A., and J.H. acknowledge support from AFOSR grant FA9550-14-1-0268. N.F. acknowledges the Stewardship Science Graduate Fellowship program's support, provided under cooperative agreement number DE-NA0002135. R.L. and S.C.W. were supported by the National Natural Science Foundation of China (No. 11274381). J.Z.M., T.Q., and H.D. were supported by the Ministry of Science and Technology of China (Nos. 2015CB921300, 2013CB921700), the National Natural Science Foundation of China (Nos. 11474340, 11234014), and the Chinese Academy of Sciences (No. XDB07000000). STM work is supported by AFOSR (FA9550-11-1-0010, DE) and NSF (DMR-1610110, ANP). This research used resources of (XPS at) the Center for Functional Nanomaterials, which is a United States Department of Energy Office of Science Facility, at Brookhaven National Laboratory under Contract No. DE-SC0012704. The NHMFL is supported by NSF through NSF-DMR-1157490 and the State of Florida.

REFERENCES

- (1) Revolinsky, E.; Beerntsen, D. J. *J. Phys. Chem. Solids* **1966**, *27*, 523–526.
- (2) Vellinga, M. B.; de Jonge, R.; Haas, C. *J. Solid State Chem.* **1970**, *2*, 299–302.
- (3) Voiry, D.; Mohite, A.; Chhowalla, M. *Chem. Soc. Rev.* **2015**, *44*, 2702–2712.
- (4) Keum, D. H.; Cho, S.; Kim, J. H.; Choe, D. H.; Sung, H. J.; Kan, M.; Kang, H.; Hwang, J. Y.; Kim, S. W.; Yang, H.; Chang, K. J.; Lee, Y. H. *Nat. Phys.* **2015**, *11*, 482–486.
- (5) Ruppert, C.; Aslan, O. B.; Heinz, T. F. *Nano Lett.* **2014**, *14*, 6231–6236.
- (6) Lezama, I. G.; Ubaldini, A.; Longobardi, M.; Giannini, E.; Renner, C.; Kuzmenko, A. B.; Morpurgo, A. F. *2D Mater.* **2014**, *1*, 021002.
- (7) Lezama, I. G.; Arora, A.; Ubaldini, A.; Barreteau, C.; Giannini, E.; Potemski, M.; Morpurgo, A. F. *Nano Lett.* **2015**, *15*, 2336–2342.
- (8) Pradhan, N. R.; Rhodes, D.; Feng, S. M.; Xin, Y.; Memaran, S.; Moon, B. H.; Terrones, H.; Terrones, M.; Balicas, L. *ACS Nano* **2014**, *8*, 5911–5920.
- (9) Lin, Y. F.; Xu, Y.; Wang, S. T.; Li, S. L.; Yamamoto, M.; Aparecido-Ferreira, A.; Li, W. W.; Sun, H. B.; Nakaharai, S.; Jian, W. B.; Ueno, K.; Tsukagoshi, K. *Adv. Mater.* **2014**, *26*, 3263–3269.
- (10) Mak, K. F.; Shan, J. *Nat. Photonics* **2016**, *10*, 216–226.
- (11) Park, J. C.; Yun, S. J.; Kim, H.; Park, J. H.; Chae, S. H.; An, S. J.; Kim, J. G.; Kim, S. M.; Kim, K. K.; Lee, Y. H. *ACS Nano* **2015**, *9*, 6548–6554.
- (12) Zhang, W.; Chiu, M. H.; Chen, C. H.; Chen, W.; Li, L. J.; Wee, A. T. S. *ACS Nano* **2014**, *8*, 8653–8661.
- (13) Cho, S.; Kim, S.; Kim, J. H.; Zhao, J.; Seok, J.; Keum, D. H.; Baik, J.; Choe, D. H.; Chang, K. J.; Suenaga, K.; Kim, S. W.; Lee, Y. H.; Yang, H. *Science* **2015**, *349*, 625–628.
- (14) Kappera, R.; Voiry, D.; Yalcin, S. E.; Branch, B.; Gupta, G.; Mohite, A. D.; Chhowalla, M. *Nat. Mater.* **2014**, *13*, 1128–1134.
- (15) Duerloo, K. A. N.; Li, Y.; Reed, E. J. *Nat. Commun.* **2014**, *5*, 4214.
- (16) Duerloo, K. A. N.; Reed, E. J. *ACS Nano* **2016**, *10*, 289–297.
- (17) Li, Y.; Duerloo, K.-A. N.; Wauson, K.; Reed, E. J. *Nat. Commun.* **2016**, *7*, 10671.
- (18) Duerloo, K.-A. N.; Reed, E. J. *ACS Nano* **2016**, *10*, 289–297.
- (19) Zhang, C. X.; Santosh, K. C.; Nie, Y. F.; Liang, C. P.; Vandenberghe, W. G.; Longo, R. C.; Zheng, Y. P.; Kong, F. T.; Hong, S.; Wallace, R. M.; Cho, K. *ACS Nano* **2016**, *10*, 7370–7375.
- (20) Qian, X. F.; Liu, J. W.; Fu, L.; Li, J. *Science* **2014**, *346*, 1344.
- (21) Soluyanov, A. A.; Gresch, D.; Wang, Z. J.; Wu, Q. S.; Troyer, M.; Dai, X.; Bernevig, B. A. *Nature* **2015**, *527*, 495–498.
- (22) Sun, Y.; Wu, S.-C.; Ali, M. N.; Felser, C.; Yan, B. *Phys. Rev. B: Condens. Matter Mater. Phys.* **2015**, *92*, 161107.
- (23) Wang, Z.; Gresch, D.; Soluyanov, A. A.; Xie, W.; Kushwaha, S.; Dai, X.; Troyer, M.; Cava, R. J.; Bernevig, B. A. *Phys. Rev. Lett.* **2016**, *117*, 056805.
- (24) Weng, H. M.; Fang, C.; Fang, Z.; Bernevig, B. A.; Dai, X. *Phys. Rev. X* **2015**, *5*, 011029.
- (25) Xu, S. Y.; Belopolski, I.; Alidoust, N.; Neupane, M.; Bian, G.; Zhang, C. L.; Sankar, R.; Chang, G. Q.; Yuan, Z. J.; Lee, C. C.; Huang, S. M.; Zheng, H.; Ma, J.; Sanchez, D. S.; Wang, B. K.; Bansil, A.; Chou, F. C.; Shibaev, P. P.; Lin, H.; Jia, S.; Hasan, M. Z. *Science* **2015**, *349*, 613–617.
- (26) Chang, T. R.; Xu, S. Y.; Chang, G.; Lee, C. C.; Huang, S. M.; Wang, B.; Bian, G.; Zheng, H.; Sanchez, D. S.; Belopolski, I.; Alidoust, N.; Neupane, M.; Bansil, A.; Jeng, H. T.; Lin, H.; Hasan, M. Z. *Nat. Commun.* **2016**, *7*, 10639.
- (27) Huang, L.; McCormick, T. M.; Ochi, M.; Zhao, Z.; Suzuki, M.-T.; Arita, R.; Wu, Y.; Mou, D.; Cao, H.; Yan, J.; Trivedi, N.; Kaminski, A. *Nat. Mater.* **2016**, *15*, 1155–1160.
- (28) Champion, J. A. *Br. J. Appl. Phys.* **1965**, *16*, 1035.
- (29) Yamamoto, M.; Wang, S. T.; Ni, M. Y.; Lin, Y. F.; Li, S. L.; Aikawa, S.; Jian, W. B.; Ueno, K.; Wakabayashi, K.; Tsukagoshi, K.; et al. *ACS Nano* **2014**, *8*, 3895–3903.
- (30) Jiang, Y. C.; Gao, J.; Wang, L. *Sci. Rep.* **2016**, *6*, 19624.
- (31) *Handbook of X-ray photoelectron spectroscopy: a reference book of standard spectra for identification and interpretation of XPS data*; Chastain, J., King, R. C., Eds.; Physical Electronics, Eden Prairie, MN, 1995.
- (32) Pletikosić, I.; Ali, M. N.; Fedorov, A. V.; Cava, R. J.; Valla, T. *Phys. Rev. Lett.* **2014**, *113*, 216601.
- (33) Rhodes, D.; Zhou, Q.; Schönmann, R.; Zhang, Q. R.; Kampert, E.; Shimura, Y.; McCandless, G. T.; Chan, J. Y.; Das, S.; Manousakis, E.; Johannes, M. D.; Balicas, L., 2016, 4, arXiv:physics/1605.09065. arXiv.org e-Print archive. <https://arxiv.org/abs/1605.09065> (accessed Aug 1, 2016).
- (34) Belopolski, I.; Xu, S. Y.; Ishida, Y.; Pan, X. C.; Yu, P.; Sanchez, D. S.; Zheng, H.; Neupane, M.; Alidoust, N.; Chang, G. Q.; Chang, T. R.; Wu, Y.; Bian, G.; Huang, S. M.; Lee, C. C.; Mou, D. X.; Huang, L. N.; Song, Y.; Wang, B. G.; Wang, G. H.; Yeh, Y. W.; Yao, N.; Rault, J. E.; Le Fevre, P.; Bertran, F.; Jeng, H. T.; Kondo, T.; Kaminski, A.; Lin, H.; Liu, Z.; Song, F. Q.; Shin, S.; Hasan, M. Z. *Phys. Rev. B: Condens. Matter Mater. Phys.* **2016**, *94*, 085127.
- (35) Lee, P. A.; Nagaosa, N.; Wen, X.-G. *Rev. Mod. Phys.* **2006**, *78*, 17–85.